Accepted Manuscript

Petroleum Geoscience

Diagenetic related flat spots within the Paleogene Sotbakken Group in the vicinity of the Senja Ridge, Barents Sea

Manzar Fawad, Nazmul Haque Mondol, Irfan Baig & Jens Jahren

DOI: https://doi.org/10.1144/petgeo2018-122

Received 7 September 2018
Revised 14 May 2019
Accepted 30 May 2019

To cite this article, please follow the guidance at http://www.geolsoc.org.uk/onlinefirst#cit_journal

Diagenetic related flat spots within the Paleogene Sotbakken Group in the vicinity of the Senja Ridge, Barents Sea

Manzar Fawad[1*], Nazmul Haque Mondol[1,2], Irfan Baig[1] & Jens Jahren[1]

[1]Department of Geosciences, University of Oslo, PO Box 1047, Blindern, 0316 Oslo, Norway
[2]Norwegian Geotechnical Institute (NGI), PO Box 3930, Ullevaal Stadion, 0855 Oslo, Norway

**Corresponding author (e-mail: manzar.fawad@geo.uio.no)*

Abstract

Rock physics analyses of data from a wildcat well 7117/9-1 drilled in the Senja Ridge area, located in the Norwegian Barents Sea, reveal a change in stiffness within the fine-grained Paleogene Sotbakken Group sediments, caused by the transformation of opal-A to opal-CT, and opal-CT to quartz. This change manifests as flat spots on 2D seismic profiles. These flat spots were mistaken as hydrocarbon-water contacts, which led to the drilling of well 7117/9-1. Rock physics analyses on this well combined with a second well (7117/9-2) drilled further northwest and updip on the Senja Ridge, indicate overpressure within the opal-CT rich zones overlying the opal-CT to quartz transformation zones in the two wells. The absence of opal-A to opal-CT and opal-CT to quartz flat spots on seismic in the second well is attributed to differences in temperature and timing of uplift. In AVA modelling, both the opal-A to opal-CT and opal-CT to quartz interface points plotted on the wet trend, whereas the modelled gas-brine, oil-brine and gas-oil contacts fell within the quadrant-I. These findings will be useful in understanding the nature of compaction of biogenic silica-rich sediments where flat spots could be misinterpreted as hydrocarbon related contacts in oil and gas exploration.

A wildcat well 7117/9-1 was drilled in 1982 on a structure located on the eastern flank of the Senja Ridge, Norwegian Barents Sea (Fig. 1). One of the incentives for this drilling location was the presence of two flat spots within assumed late Cretaceous sandstone reservoirs (NPD 2018). However, after drilling, both flat spots were found to be within the Paleocene claystones of the Sotbakken Group. A core taken from 1355 to 1365.6 m (MDRKB) just below the upper flat spot revealed the presence of horizontal bands of amorphous silica (chert) within the claystone. The secondary objective, originally considered to be middle to early Jurassic sediments, was instead found to consist of Cretaceous silty claystones. The well was declared dry (NPD 2018). A second wildcat well 7117/9-2 was drilled in 1983 on the Senja Ridge, updip and about 5.6 km north-west of well 7117/9-1. The vicinity of the second well did not show the presence of the flat spots, and the primary and secondary objectives were selected deeper than the Sotbakken Group interval. This well also failed to find hydrocarbon-bearing reservoirs and was proclaimed dry.

The Paleogene Sotbakken Group comprises the Torsk Formation (Fig. 2) which consists of light to medium grey or greenish-grey, generally non-calcareous claystones. Rare siltstone/limestone stringers occur throughout the unit (NPD 2018). The Torsk Formation mudstones were deposited in a deep marine shelf setting, with no significant coarse clastic sediment input (Dalland 1988). Deep marine mudstones may contain substantial amounts of biogenic silica (opal-A), particularly radiolaria, diatoms and siliceous sponges, in areas with high organic productivity (Bjørlykke 2015). Diagenetic reactions of biosiliceous sediment occur at shallow depths (<1000 m) and low temperature (<50 °C) during burial (Ireland *et al.* 2010). Initially, opal-A (biogenic silica) dissolves and precipitates as opal-CT (crystalline silica); this is followed by the transformation of opal-CT to quartz at greater burial depths and temperatures of about 60-80 °C (Isaacs 1982; Williams & Crerar 1985; Ireland *et al.* 2010, Bjørlykke 2015). The rate of transformation of opal-A to opal-CT depends on temperature and time, and may reduce total sediment porosity by as much as 30% (Kastner et al. 1977; Isaacs 1981; Tada & Iijima 1983; Wrona *et al.* 2017), in the process releasing large volumes of pore water and resulting in increased stiffness (Peltonen *et al.* 2008; Marcussen *et al.* 2009; Thyberg *et al.* 2009) and a substantial acoustic impedance contrast. Ishii *et al.* (2011) found that within the transition zone between opal-A and opal-CT, dispersed microcrystalline opal-CT precipitates coexist with an original diatom-supported framework, forming a mechanically "hard zone". Below the "hard zone," the opal-A framework is lost and replaced by opal-CT aggregates. The strength of the "hard zone" probably reflects the strong framework/cementation due to the coexistence of opal-A and opal-CT. Depending upon the

"hard zone" thickness and seismic resolution a seismic reflection interface could generate that may cross-cut stratigraphy (Hein *et al.* 1978). It could also result in the transition zone between opal-A and opal-CT becoming brittle. Within such brittle zones, deformation could result in the formation of fluid conduits. Below the "hard zone", where the opal-A framework strength is lost, increased clay compaction is expected compared to the zone above the transition zone, associated with the release of considerable amounts of compaction fluids. A variety of fluid flow conduits detected within and above the opal-A to opal-CT reaction zone are evidence of water expulsion from the opal-A to the opal-CT reaction zone, and transient upward flow (Davies *et al.* 2008).

The development of the opal-A to opal-CT transformation has been categorized in three phases: (1) formation, (2) migration, (3) fossilisation (Davies & Cartwright 2002; Wrona *et al.* 2017). This division is based on the spatial and temporal settings, and controls on the opal-A to opal-CT transformation in the North Viking Graben, northern North Sea. The opal-A to opal-CT transformation zone is considered to be the point when a minimum transformation temperature has been reached. A fossilised opal-A to opal-CT interface manifested as a flat spot represents the point when the migration rate becomes zero despite the presence of opal-A in the overlying strata (Wrona *et al.* 2017).

The main objective of this paper is to investigate the effect of silica transformation on elastic and physical properties of the Sotbakken Group rocks. The mechanical and then chemical compaction with increasing depth, temperature and time result in changes in the rock microfabric and stiffness, whice have a direct influence on the physical properties such as resistivity, and the elastic properties i.e. P –wave velocity (Vp), S –wave velocity (Vs) and density. The results of this study will aid the identification of diagenetic related flat spots prior to drilling and identification of various silica transformation stages after drilling.

Geological setting

The Senja Ridge study area is located towards the western margin basins of the Barents Sea, with the Tromsø Basin to the east, the Sørvestsnaget Basin to the west and the Harstad Basin to the south (Fig.1). The Senja Ridge itself is an NNE-SSW trending intra-basinal high, which defines the western limit of the Tromsø Basin (Faleide *et al.* 1993). It was a positive structural element from the mid-Cretaceous and has a positive gravity anomaly indicating a shallow basement (Gabrielsen *et al.* 1990; Riis 1996). The relief on the ridge is due to Late Cretaceous to early Cenozoic normal faulting and salt mobilization in the Tromsø Basin (Faleide *et al.* 1993).

The Tromsø Basin is a NNE-SSW oriented deep Cretaceous basin (Faleide *et al.* 1984; Gabrielsen *et al.* 1990). The basin contains several salt structures (Faleide *et al.* 1993; Smelror *et al.* 2009). The basin was a part of a larger, regional basin in pre-Jurassic times. Clastic deposition occurred during the Triassic in a relatively quiet period, characterized by regional subsidence. The development of a separate basin was initiated in the Jurassic. During the Cretaceous, the sediments were deposited with contemporaneous subsidence and salt movements (Faleide *et al.* 1984). This eventually led to most of the basin being infilled, prior to becoming part of the regionally subsiding basin during the late Cretaceous. In the Cenozoic, it acted as one of the main depocentres in the southwestern Barents Sea (Gabrielsen *et al.* 1990).

In the middle Oligocene, large areas of the Barents Shelf east of the Senja Ridge were uplifted due to a shift in tectonic regime (NPD 2018). The shelf was subjected to erosion, which lasted until the Pliocene (Ryseth *et al.* 2003). This erosion resulted in the removal of the upper part of the Sotbakken Group in the eastern parts of Tromsø Basin. The lower parts of the Group are probably present across the Barents Shelf; however, the younger sediments are only preserved over the Ringvassøy - Loppa Fault Complex and in the Tromsø Basin (Spencer *et al.* 1984).

Since the area of interest is located at the western edge of the Barents Sea, there is only limited to moderate uplift (0 to 1000 m, Table 1) according to previous studies (e.g. Riis & Fjeldskaar 1992; Ohm *et al.* 2008; Henriksen *et al.* 2011; Baig *et al.* 2016; Ktenas *et al.* 2017). However, the disparity between the uplift values between different studies is noticeable, owing possibly to the various methods employed. Ohm *et al.* (2008) and Henriksen *et al.* (2011) suggested no exhumation in the areas of the Senja Ridge and the western margin of Tromsø Basin, whereas, Riis & Fjeldskaar (1992), Baig *et al.* (2016) and Ktenas *et al.* (2017) suggested moderate exhumation (250-1000 m) in these areas (Fig. 3).

Materials and methods

The study is based on data from two dry wells 7117/9-1 and 7117/9-2 in the Senja Ridge area of the Barents Sea (Fig. 1). Five 2D seismic lines from the AMR-NBR survey were available. The seismic data quality varies from fair to good. XRD analysis data on silica phase transformation from well 7117/9-1 was digitized from a petrographic report (Roaldset & He 1995). The present-day temperature gradient was calculated from the bottom hole temperature (BHT) data (NPD 2018) and compared with the paleotemperature estimated from vitrinite reflectance (VR) data by using the following equations:

$$T_{max} = (\ln R_o + 1.68)/0.0124 \quad \text{(Barker \& Pawlewicz 1994)} \qquad \ldots\ldots\ldots\ldots\ldots \qquad (1)$$

$$T_{max} = (\ln R_o + 1.4)/0.0096 \quad \text{(Corcoran \& Clayton 1999)} \qquad \ldots\ldots\ldots\ldots\ldots \qquad (2)$$

Vitrinite reflectance data points are available from depths greater than 1400 m (MDRKB) in both wells 7117/9-1 and 7117/9-2. Only a single vitrinite reflectance data point was available within the Sotbakken Group in well 7117/9-1, and no vitrinite reflectance data was available within the Sotbakken Group in well 7117/9-2. Therefore, paleotemperature was calculated from available vitrinite reflectance data points to estimate the paleotemperature gradient in both wells (Table 2). This paleotemperature gradient was then used to extrapolate maximum paleotemperature at the top and base of Sotbakken Group (Table 3) by using the uplift and erosion estimates from Baig *et al.* (2016).

Selected slabs were available from the core that was cut from 1355 m to 1365.6 m (MDRKB) in the well 7117/9-1. Four samples for SEM analysis were taken at depths 1357.84 m, 1360.4 m, 1363.47 m and 1363.75 m (MDRKB). The slides were prepared perpendicular to the bedding. We had no access to the cutting samples and/or side wall cores taken in the two wells.

A stratigraphic correlation between the two wells (7117/9-1 and 7117/9-2) is shown in Fig. 4. Tops of the lithostratigraphic Groups were taken from NPD (2018). Only the top Sotbakken Group was correlated a little deeper at the high gamma ray spike, indicating an unconformity, and coinciding with a prominent trough on seismic. The seismic data polarity was SEG normal, i.e. a peak represented an increase in acoustic impedance.

For AVA (amplitude vs. angle) analysis the logs were blocked with a 10 m interval to reduce the scatter in the data. Since S-wave logs were not acquired, the "mudrock equation" (Castagna et al., 1985) was used, assuming a 50:50 quartz to clay ratio, to generate an "in-situ" shear wave curve. A wavelet was extracted using seismic line AMR_NBR08-135652 and AVA synthetics were generated using the Zoeppritz equation (Zoeppritz 1919).

To compare with the fluid related contact AVA (amplitude vs. angle) responses, a shallow aquifer at 1300 m MDRKB in a well from the North Sea was used to model the gas-water, oil-water and gas-oil contacts (Fig. 5). Synthetic S-wave velocity logs were generated using Greenberg and Castagna (1992) method. The elastic property logs (i.e., P –wave velocity (Vp), S –wave velocity (Vs) and Density) were blocked using Backus averaging. A window of 40 m was found appropriate for blocking to reduce the effect of lithological interfaces. The fluid properties of water and hydrocarbon were calculated using FLAG 2014 and FLAG 2014 Global methods respectively. The software default fluid properties were used, i.e. oil gravity= 30 API, GOR = 100 L/L and gas gravity= 0.6. The water salinity used was 10000 ppm with NaCl=100%. Since the sandstone aquifer is at 1200 m, a temperature 38° C and pressure 12 MPa was used for the AVA modelling of the various fluid interfaces.

Scanning electron microscopy (SEM)

Samples for SEM were stabilized with epoxy and slides were produced from slices cut from the core. The slides were carbon coated and studied in a HITACHI SU5000 Scanning Electron Microscope

(SEM) equipped with a XFlash30 EDS system capable of spectral identification and elemental mapping. Photographs were captured as backscattered images for each slide.

Observations and results

Physical properties related to mineralogy

On the seismic line AMR_NBR08-135652 passing through well 7117/9-1, both the opal-A to opal-CT and opal-CT to quartz flat spots are evident (Fig. 6). These flat spots do not extend updip towards well 7117/9-2 in the northwest (Fig. 7).

A comparison of physical and elastic properties i.e. gamma ray, deep resistivity, acoustic impedance, present-day temperature and mineralogy from XRD analysis (Roaldset & He 1995) in well 7117/9-1 are shown in Figure 8. Observing the general resistivity trends from the shallowest readings in the wells, ignoring local anomalies, a gradual decrease in resistivity in both wells were observed to an inflection point situated above the base of the Sotbakken Group (Figs. 4 and 8). The overall drop in resistivity in well 7117/9-1 was about 2.2 ohm-m over a depth interval of 1240 m, whereas in well 7117/9-2 the resistivity dropped by 3.5 ohm-m over a depth interval of 1000 m to the inflection point (Fig. 8). Under a normal compaction regime, the general resistivity trend is expected to increase with depth.

The opal-A to opal-CT interface (Fig. 8) in well 7117/9-1 was exposed to an estimated 51°C paleotemperature and the hard event shows an increase of about 1080 g/cm^3*m/s acoustic impedance, caused by an increase of about 290 m/s P-wave velocity (Vp) and 0.25 g/cm^3 bulk density (RHOB). The opal-CT to quartz boundary experienced a maximum temperature of 65°C and the interface exhibited an increase of 1070 g/cm^3*m/s acoustic impedance (AI), as a result of 300 m/s and 0.2 g/cm^3 increase in Vp and RHOB respectively.

The core taken in the well 7117/9-1 just below the opal-A to opal-CT boundary consists of mudstones with strong lineations of light (chert) and dark (clay) minerals. Analysis of the light bands with the SEM reveals voids filled with circa 2 µm opal-CT granular spheres, with the presence of occasional opal-A grains (Fig. 9). Sporadic pyrite is also evident, possibly formed from sulfate reduction.

In well 7117/9-2 neither the opal-A to opal-CT nor the opal-CT to quartz boundaries are evident within the Sotbakken Group interval, both on seismic and in the well logs. The top Sotbakken Group is calculated to have been exposed to 48°C paleotemperature, whereas the base Sotbakken Group experienced a maximum temperature of 57° C (Fig. 4).

Bulk density-Vp cross plots

Comparison of data from the two wells (7117/9-1 and 7117/9-2) on the density and Vp cross plot shows that the Sotbakken Group at a shallower depths in well 7117/9-2 has both lower density and

lower Vp (Fig. 10a), and corresponding to lower temperatures, as compared to well 7117/9-1 (Fig. 10b).

The RHOB-Vp cross plot of well 7117/9-1 shows three distinct trends (Figs 11a and 11b), generally there is a systematic increase of bulk density and Vp with an increase in depth. However the cluster with high gradient, plotting within 2050 m/s to 2250 m/s velocity limits, shows an inversion i.e. the RHOB-Vp values decrease with depth and temperature. The whole Sotbakken package within well 7117/9-2 showed a similar inversion (similar to the high gradient cluster in well 7117/9-1) i.e. the RHOB-Vp decreased with depth and temperature (Figs. 11c and 11d).

The RHOB-Vp data colour-coded with quartz percentage (Fig. 12a) and opal-CT (Fig. 12b) from the XRD analysis confirmed two "knees" in the data trend signifying the transition from opal-A to opal-CT and from opal-CT to quartz.

Discussion

Influence of mechanical and chemical compaction on physical and elastic properties of biogenic silica rich sediments

The SEM analysis from the core taken below the opal-A to opal-CT boundary shows that the chert contains abundant voids with transformed opal-CT granules (Fig. 9). If one follows the findings of Ishii *et al.* (2011) a possible stiffening model would allow the formation of a "hard zone" by cementation of the opal-A framework by neo-formation of dispersed opal-CT particles during the early part of the transformation from opal-A to opal-CT. From the 7117/9-1 well acoustic impedance curve, the hard zone is approximately 21 m thick. Assuming a frequency of 40 Hz with average seismic velocity of 2100 m/s the seismic resolution around this depth is 13 m. The interface caused about 1080 g/cm^3*m/s acoustic impedance increase resulting in a flat spot in the area of well 7117/9-1. While subsidence, the hard zone is lost during the later part of the opal-A to opal-CT transformation as the remaining opal-A framework (the fossils) is lost and replaced by localized clusters of opal-CT. At this stage increased compaction due to framework collapse may also result in increased clay compaction and possible increased density, or undercompaction associated with fluid overpressure if the permeability is low.

Within the opal-CT rich zone in well 7117/9-1 and in the whole Sotbakken Group in well 7117/9-2 , the decrease in Vp and RHOB with depth (Figs. 11 and 12) indicate overpressure in these intervals. Overpressure was also documented from 1600 m to 1700 m (MDRKB) in the well 7117/9-1 drilling report (NPD 2018). The bad hole condition in both the wells through the above intervals, reflected by the poor caliper data, further strengthen this inference, as overpressured mudstones tend to collapse in the well bore.

The hard event at the opal-CT to quartz transformation zone that was exposed to a maximum temperature of 65°C demonstrated an increase of 1070 g/cm^3*m/s in acoustic impedance (AI). This transformation may be related to recrystallization of the dispersed opal-CT particles formed during early stage opal-A to opal-CT transformation within the fine-grained sediment to micro quartz. Micro quartz is known to have a stiffening effect during cement formation (Thyberg *et al.* 2010, Thyberg & Jahren 2011). In addition, dispersed neo-formed micro quartz sourced from the dissolution of opal-CT clusters may increase sediment stiffness across the narrow opal-CT micro quartz transition zone. The reason for neo-formation of both dispersed fine-grained opal-CT during initial opal-A to the opal-CT formation and dispersed micro quartz from opal-CT would be silica supersaturation at or above nucleation levels within the whole sediment volume during the initial stages of both reactions. This dispersed micro-quartz formation stage is even seen in porous sandstones where microquartz nucleation sourced from opal-CT clusters take place in systems totally dominated by macro-crystalline quartz surfaces resulting in pervasive micro-quartz coatings (Aase et al 1995, Jahren and Ramm 2000). The cementing effect documented between illitic clays and micro-quartz (Thyberg et al 2010) show that even clay dominated sediments contain suitable substrates for micro-quartz formation resulting in the observed rock stiffening. A sequence of deposition of amorphous silica nanofilm followed by chalcedony crystallization could also form nucleation points for microcrystalline quartz (French *et al*. 2012), resulting in quartz cementation and stiffness increase in sandstones. More detailed SEM work on core and cuttings samples is needed to verify the above-suggested mechanisms.

The gradual decrease in the deep resistivity (HRD) from shallow depths to an inflection point above the base of the Sotbakken Group can be caused by a combination of transition of pore fluids from marine saline Sotbakken Group deposits to more glacial fresh water dominated Nordland Group sediments, and overpressure within the Sotbakken Group. The inflection point in resistivity (Figs 4 and 8) below which the values start increasing with depth could indicate the onset of quartz cementation. The HRD and AI trends indicate that formation of opal CT from opal-A is gradual between 1300m and 1700m and that the Opal –CT to quartz transition is sharp around 1700m demonstrating the time-temperature effect (Fig 8).

The decrease in resistivity within the Sotbakken Group in well 7117/9-2 from the opal-A to opal-CT boundary to the resistivity inflection point was about 0.46 ohm-m corresponding with an AI decrease of 670 g/cm^3*m/s (Fig. 4), whereas the decrease in resistivity in well 7117/9-1 within the Sotbakken Group from the opal-A to opal-CT boundary to the resistivity inflection point was about 0.46 ohm-m corresponding with an AI decrease of 940 g/cm^3*m/s (Fig. 8). Therefore, the deep resistivity-AI cross plots within the Sotbakken package discriminate various facies (Fig. 13), which can be useful for analyzing similar diagenetic environment. The trend -1 in well 7117/9-1 represents amorphous silica mechanical compaction followed by chemical compaction (Fig. 13a). This trend is manifested by increasing deep resistivity with increasing acoustic impedance until a high point is

reached. This is possibly the hard event where both opal-A and opal-CT coexist. The subsequent trend (Trend 2) manifests the opal-CT transformation where the framework is replaced by fine opal-CT aggregates. The gradual reduction of HRD and AI reflect a decrease in compaction possibly due to increasing overpressure. The final trend (Trend 3) likely starts with the onset of quartz cementation and the deep resistivity increases with increase in AI as the quartz cement increase with temperature as a function of depth. In well 7117/9-2 the trend 1is absent (Fig. 13b), however, the opal-CT transformation zone is represented by a decrease of resistivity with a decrease of acoustic impedance due to a possible increase in pore pressure indicating low permeability while expulsion of water taking place within the opal-CT transition zone. Trend 3 shows the increase of resistivity with increasing acoustic impedance representing the onset of quartz cementation.

Both the opal-A to opal-CT and opal-CT to quartz boundaries show a very weak Type-1 AVA signatures (Rutherford & Williams 1989) (Fig. 14a). As mentioned earlier both the interfaces cause hard events represented by (red) peaks. With the increase in the incident angle, the peak's amplitude gradually reduces, but the reduction magnitude is negligible. As expected the opal-A to opal-CT and opal-CT to quartz interface points plot on the background wet line in the Intercept-Gradient cross plot (Castagna & Swan 1997; Castagna *et al*. 1998). Not much literature is available on the gas/oil/water contact AVA's, therefore we attempted to model AVAs of various fluid contacts within a North Sea aquifer by fluid substitution technique (Gassmann 1951) (Fig. 5). The aquifer had undergone an estimated uplift of 500-1000 m with present-day depth of ~1300 m MDRKB, the similar depth of sediments this study deals with. All the three fluid related interfaces, i.e. gas-water, oil-water and gas-oil contacts showed a weak positive gradient on the amplitude vs. angle plane (Fig. 15a). The magnitude of intercepts of the fluid contacts are not so distinct compared to that of opal-A to opal-CT, however, the points plot within quadrant-I within the intercept-gradient cross-plot (Fig. 15b). The actual AVA analysis of this type of response will possibly not be meaningful owing to the magnitude falling within the error limits and noise. The sand reservoir/aquifer has a very high P-wave velocity, i.e. around 2800 m at 1300 m depth. It can be inferred that the reservoir had undergone a high level of quartz cementation at maximum burial depth. This could be a reason of AVA response subdued because of high stiffness. A reservoir at a shallow depth not experiencing much chemical compaction is expected to show similar AVA signatures but with high magnitude enabling to differentiate a fluid interface related anomaly from that of a diagenetic related anomaly.

Temperature changes due to uplift

Assuming the present day temperature gradient in well 7117/9-1, the opal-A to opal-CT interface/transition lies at about 44°C (Fig. 3) and the temperature at the opal-CT to quartz boundary is 58°C. After compensating for the maximum uplift (Baig *et al*. 2016, Table 1) i.e. 250m, the rocks

would have experienced an additional 7°C. In this case, resulting temperatures would become 51°C for the opal-A to opal-CT boundary and 65°C for the opal-CT to quartz boundary.

On the seismic profile (Fig. 7), the opal-A to opal-CT boundary does not appear to extend towards the northwest towards well 7117/9-2. The base Sotbakken group lies at an estimated present-day temperature of 44°C. Assuming a maximum uplift of 460m (reported by Baig *et al*. 2016) using well 7117/9-2, the additional temperature the rocks were exposed to was 13°C, making the estimated temperature at the base of Sotbakken Group of about 57°C. Although the Sotbakken Group package was exposed to temperatures suitable for opal-A to opal-CT transformation (>51°C from 7117/9-1), the absence of this interface on seismic can be explained as follows. .

Timing of events

As the opal-A to opal-CT and opal-CT to quartz boundaries are cross-cutting the Sotbakken Group bedding planes (Fig. 6b), therefore both the boundaries were probably developed post uplift of the Senja ridge. The overlying Nordland Group sediments onlap on the anticlinal structure marked by top Sotbakken Group (Fig. 6b). The increase in thickness of the Nordland Group pushed the underlying Sotbakken package gradually through the time and temperature suitable for the Opal-A to opal-CT transformation and then the opal-CT to quartz transformation. The compaction related fault F1 (Fig 6b) does not extend above the top Sotbakken Group. However, it cuts across and slightly displaces the opal-CT to quartz boundary showing that it possibly formed during the chemical reactions taking place and continued after the flat spot was formed. These types of faults provide conduits for water squeezed from the pores as a result of chemical compaction (Davies *et al*. 2008). The displacement of the Sotbakken Group top against the fault is more than the displacement of the opal-CT to quartz boundary indicating significant compaction within the opal-CT zone compared to beneath the opal-CT to quartz boundary. The fault does not extend above the Sotbakken Group boundary possibly as the overlying sediments were less compacted and dissipated the emanated water.

The reason for the absence of the opal-A to opal-CT boundary cross-cutting the bedding in the seismic profile (Fig. 7a) within the vicinity of the 7117/9-2 well could be because this area was flat compared to a gentle anticline at 7117/9-1 well location. The opal-A to opal-CT boundary was possibly formed parallel to the bedding in the well 7117/9-2 area. The lower contact of the Sotbakken Group was exposed to maximum 57°C, so the opal-CT to quartz boundary would have formed deeper within the formations below, as evidenced by the increase in AI within the Nygrunnen Group (Fig. 4). A subsequent uplift in the vicinity of well 7117/9-2 could have truncated the opal-A to the opal-CT boundary on the apex of the anticline leaving the opal-CT rich package within the Sotbakken Group. The alternate explanation regarding the absence of biogenic silica is not plausible as the distance between the two wells is only 5.6 km. Also, the presence of high pore pressure similar to the opal-CT rich zone in the well 7117/9-1 strengthens the same mineralogy model.

Conclusions

Well 7117/9-1 penetrated both opal-A to opal-CT and opal-CT to quartz transformation zones. The opal-CT rich zones in both the wells 7117/9-1 and 7117/9-2 were over-pressured due to the expulsion of water from the silica transformation reactions.

The opal-A to opal-CT interface is interpreted as a possible stiffening by cementation of the opal-A framework by neoformation of dispersed opal-CT particles in the early part of the transformation. The opal-CT to quartz interface flat spot formation may be explained by a stiffening related to the transformation of dispersed Opal- CT particles into micro quartz (indicating dispersed growth of Opal-CT at the opal-A/CT transition zone) or/and the possibility of neoformation of dispersed micro-quartz from recrystallization of localized opal-CT aggregates (stiffening from dispersed micro quartz formed from non-dispersed opal-CT flocks).

AVA modelling of the opal-A to opal-CT and opal-CT to quartz interfaces confirm that both the transformation points plot on the wet trend, however the gas-water, oil-water and gas-oil contact points plotted within the quadrant-I above the wet trend. Reservoirs with low quartz cementation are expected to generate distinct AVA signatures from that of diagenetic related interfaces. In case of highly cemented sandstone reservoir, the AVA difference was within the error and noise limits.

The absence of an extension of both the opal-A to opal-CT and opal-CT to quartz related flat spots from well 7117/9-1 to 7117/9-2 towards northwest is possibly due to the difference in timing of uplift and temperature between the two structures.

Acknowledgements

The authors are grateful for the support and funding provided by Eni Norge for the SEALCAP (Shale rock properties and sealing capacity in the SW Barents Sea area) project, that was an R&D collaboration between the University of Oslo and Norwegian Geotechnical Institute (NGI). The authors thank the University of Oslo (UiO) for providing the sample material, equipment support and facilitation to publish this paper. Academic software licenses have been provided by Lloyd's Register for Interactive Petrophysics (IP™), CGG for Hampson-Russell (HRS™), and Schlumberger for Petrel™. The authors would like to thank the editor and the reviewers for their time and valuable input.

References

Aase, N.E., Bjorkum, P.A. & Nadeau, P.H. 1996. The effect of grain-coating microquartz on preservation of reservoir porosity. *AAPG bulletin*, **80**, 1654–1673.

Baig, I., Faleide, J.I., Jahren, J. & Mondol, N.H. 2016. Cenozoic exhumation on the southwestern Barents Shelf: Estimates and uncertainties constrained from compaction and thermal maturity analyses. *Marine and Petroleum Geology*, **73**, 105–130.

Barker, C.E. & Pawlewicz, M.J. 1994. Calculation of vitrinite reflectance from thermal histories and peak temperatures: a comparison of methods. ACS Publications.

Bjørlykke, K. 2015. *Petroleum Geoscience, From Sedimentary Environments to Rock Physics*, Second Edition.

Castagna, J.P. & Swan, H.W. 1997. Principles of AVO crossplotting. *The leading edge*, **16**, 337–344.

Castagna, J.P., Batzle, M.L. & Eastwood, R.L. 1985. Relationships between compressional-wave and shear-wave velocities in clastic silicate rocks. *Geophysics*, **50**, 571–581.

Castagna, J.P., Swan, H.W. & Foster, D.J. 1998. Framework for AVO gradient and intercept interpretation. *Geophysics*, **63**, 948–956.

Corcoran, D. & Clayton, G. 1999. Interpretation of vitrinite reflectance profiles in the Central Irish Sea area: implications for the timing of organic maturation. *Journal of Petroleum Geology*, **22**, 261–286.

Dalland, A. 1988. A lithostratigraphic scheme for the Mesozoic and Cenozoic succession offshore Norway north of 62° N. *Norw. Petrol. Dir. Bull.*

Davies, R.J. & Cartwright, J. 2002. A fossilized Opal A to Opal C/T transformation on the northeast Atlantic margin: Support for a significantly elevated palaeogeothermal gradient during the Neogene? *Basin Research*, **14**, 467–486.

Davies, R.J., Goulty, N.R. & Meadows, D. 2008. Fluid flow due to the advance of basin-scale silica reaction zones. *Geological Society of America Bulletin*, **120**, 195–206.

Faleide, J.I., Gudlaugsson, S.T. & Jacquart, G. 1984. Evolution of the western Barents Sea. *Marine and Petroleum Geology*, **1**, 123–150.

Faleide, J.I., Vågnes, E. & Gudlaugsson, S.T. 1993. Late Mesozoic-Cenozoic evolution of the south-western Barents Sea in a regional rift-shear tectonic setting. *Marine and Petroleum Geology*, **10**, 186–214.

French, M.W., Worden, R.H., Mariani, E., Larese, R.E., Mueller, R.R. & Kliewer, C.E. 2012. Microcrystalline quartz generation and the preservation of porosity in sandstones: Evidence from the Upper Cretaceous of the Subhercynian Basin, Germany. *Journal of Sedimentary Research*, **82**, 422–434.

Gabrielsen, R.H., Færseth, R.R., Jensen, L.N, Kalheim, J.E & Riis, F. 1990. Structural elements of the Norwegian Continental Shelf, Part 1, the Barents Sea Region. *Norwegian Petroleum Directorate Bulletin 6. Norwegian Petroleum Directorate, Stavanger*, 1–33.

Gassmann, F. 1951. Über die elastizität poröser medien: *Vierteljahrss-chrift der Naturforschenden Gesellschaft in Zurich*, **96**, 1-23. Paper translation at http://sepwww. stanford. edu/sep/berryman/PS/gassmann. pdf.

Greenberg, M.L. & Castagna, J.P. 1992. Shear- wave velocity estimation in porous rocks: Theoretical formulation, preliminary verification and applications. *Geophysical prospecting*, **40**, 195–209.

Hein, J.R., Scholl, D.W., Barron, J.A., Jones, M.G. & Miller, J. 1978. Diagenesis of late Cenozoic diatomaceous deposits and formation of the bottom simulating reflector in the southern Bering Sea. *Sedimentology*, **25**, 155–181.

Henriksen, E., Bjørnseth, H.M., et al. 2011. Uplift and erosion of the greater Barents Sea: impact on prospectivity and petroleum systems. *Geological Society, London, Memoirs*, **35**, 271–281.

Ireland, M.T., Goulty, N.R. & Davies, R.J. 2010. Influence of pore water chemistry on silica diagenesis: evidence from the interaction of diagenetic reaction zones with polygonal fault systems. *Journal of the Geological Society*, **167**, 273–279.

Isaacs, C.M. 1981. Porosity reduction during diagenesis of the Monterey Formation, Santa Barbara coastal area, California.

Isaacs, C.M. 1982. Influence of rock composition on kinetics of silica phase changes in the Monterey Formation, Santa Barbara area, California. *Geology*, **10**, 304–308.

Ishii, E., Sanada, H., Iwatsuki, T., Sugita, Y. & Kurikami, H. 2011. Mechanical strength of the transition zone at the boundary between opal-A and opal-CT zones in siliceous rocks. *Engineering geology*, **122**, 215–221.

Jahren, J. & Ramm, M. 2000. The porosity-preserving effects of microcrystalline quartz coatings in arenitic sandstones: Examples from the Norwegian continental shelf. *Quartz cementation in sandstones*, **29**, 271–280.

Kastner, M., Keene, J.B. & Gieskes, J.M. 1977. Diagenesis of siliceous oozes—I. Chemical controls on the rate of opal-A to opal-CT transformation—an experimental study. *Geochimica et Cosmochimica Acta*, **41**, 1041–1059.

Ktenas, D., Henriksen, E., Meisingset, I., Nielsen, J.K. & Andreassen, K. 2017. Quantification of the magnitude of net erosion in the southwest Barents Sea using sonic velocities and compaction trends in shales and sandstones. *Marine and Petroleum Geology*, **88**, 826–844.

Marcussen, Ø., Thyberg, B.I., Peltonen, C., Jahren, J., Bjørlykke, K. & Faleide, J.I. 2009. Physical properties of Cenozoic mudstones from the northern North Sea: Impact of clay mineralogy on compaction trends. *AAPG Bulletin*, **93**, 127–150.

Moe, H.R., Roaldset, E. & Gjesvik, N. 1988. Silicious sediments and seismic responses – A correlation tool on Norwegian Shelf. *(Unpublished manuscript)*.

NPD. 2014. Norwegian Petroleum Directorate Lithostratigraphic chart, Norwegian Barents Sea.http://www.npd.no/Global/Engelsk/2-Topics/Geology/Lithostratigraphy/BH-OD1409003.pdf.

NPD. 2018. Norwegian Petroleum Directorate Fact-pages.http://www.npd.no/engelsk/cwi/pbl/en/index.htm.

Ohm, S.E., Karlsen, D.A. & Austin, T.J.F. 2008. Geochemically driven exploration models in uplifted areas: Examples from the Norwegian Barents Sea. *AAPG bulletin*, **92**, 1191–1223.

Peltonen, C., Marcussen, Ø., Bjørlykke, K. & Jahren, J. 2008. Mineralogical control on mudstone compaction: a study of Late Cretaceous to Early Tertiary mudstones of the Vøring and Møre basins, Norwegian Sea. *Petroleum Geoscience*, **14**, 127–138.

Riis, F. 1996. Quantification of Cenozoic vertical movements of Scandinavia by correlation of morphological surfaces with offshore data. *Global and Planetary Change*, **12**, 331–357.

Riis, F. & Fjeldskaar, W. 1992. On the magnitude of the Late Tertiary and Quaternary erosion and its significance for the uplift of Scandinavia and the Barents Sea. *Structural and tectonic modelling and its application to petroleum geology*, **1**, 163–185.

Roaldset, E. & He, W. 1995. Silica-phase transformation of opal-A to opal-CT to quartz—an experimental approach. *Report: Department of Geology and Mineral Resources Engineering, Norwegian Institute of Technology, Trondheim*.

Rutherford, S.R. & Williams, R.H. 1989. Amplitude-versus-offset variations in gas sands. *Geophysics*, **54**, 680–688.

Ryseth, A., Augustson, J.H., et al. 2003. Cenozoic stratigraphy and evolution of the Sørvestsnaget Basin, southwestern Barents Sea. *Norwegian Journal of Geology/Norsk Geologisk Forening*, **83**.

Smelror, M., Petrov, O.V., Larssen, G.B. & Werner, S.C. 2009. Geological history of the Barents Sea. *Norges Geol. undersøkelse*, 1–135.

Spencer, A.M., Home, P.C. & Berglund, L.T. 1984. Tertiary structural development of the western Barents Shelf: Troms to Svalbard. *In*: *Petroleum Geology of the North European Margin*. Springer, 199–209.

Tada, R. & Iijima, A. 1983. Petrology and diagenetic changes of Neogene siliceous rocks in northern Japan. *Journal of Sedimentary Research*, **53**, 911–930.

Thyberg, B. & Jahren, J. 2011. Quartz cementation in mudstones: sheet-like quartz cement from clay mineral reactions during burial. *Petroleum Geoscience*, **17**, 53–63.

Thyberg, B., Jahren, J., Winje, T., Bjørlykke, K. & Faleide, J.I. 2009. From mud to shale: Rock stiffening by micro-quartz cementation. *First Break*, **27**, 53–59.

Thyberg, B., Jahren, J., Winje, T., Bjørlykke, K., Faleide, J.I. & Marcussen, Ø. 2010. Quartz cementation in Late Cretaceous mudstones, northern North Sea: changes in rock properties due to dissolution of smectite and precipitation of micro-quartz crystals. *Marine and Petroleum Geology*, **27**, 1752–1764.

Williams, L.A. & Crerar, D.A. 1985. Silica diagenesis; II, General mechanisms. *Journal of Sedimentary Research*, **55**, 312–321.

Wrona, T., Jackson, C.A.-L., Huuse, M. & Taylor, K.G. 2017. Silica diagenesis in Cenozoic mudstones of the North Viking Graben: physical properties and basin modelling. *Basin Research*, **29**, 556–575.

Zoeppritz, K. 1919. VII b. Über Reflexion und Durchgang seismischer Wellen durch Unstetigkeitsflächen. *Nachrichten von der Gesellschaft der Wissenschaften zu Göttingen, Mathematisch-Physikalische Klasse*, **1919**, 66–84.

Figure captions

Fig. 1. Location and geological setting of Senja ridge. Five 2D seismic lines used in this study are shown. (Modified from Baig et al. 2016, structural elements are from Gabrielsen *et al.* 1990). NB: Nordkapp Basin, ND: Norvang Dome, RLFC: Ringvassøy-Loppa Fault Complex SD: Samson Dome, SvD: Svalis Dome.

Fig. 2. Lithostratigraphic nomenclature for the Norwegian Barents Sea (From NPD 2014). The red rectangle indicates the relevant succession for our area of interest.

Fig. 3. Map illustrating the total amount of uplift from compaction and thermal maturity based techniques. The area of interest is marked by the red rectangle (Modified from Baig et al. 2016, structural elements are from Gabrielsen *et al.* 1990). NB: Nordkapp Basin, ND: Norvang Dome, SD: Samson Dome, SR: Senja Ridge, SvD: Svalis Dome.

Fig. 4. Cross section between well 7117/9-1 and 7117/9-2 hung on mean sea level (MSL) as datum. The present-day temperature curve has been computed using the bottom hole temperature data, whereas the paleotemperature is calculated using vitrinite reflectance (VR). A gradual decrease in the resistivity log value can be observed in both the wells which at a certain depth ("inflection point", indicated by black arrow) starts increasing with depth.

Fig. 5. Fluid replacement modelling and resulting changes in the P –wave velocities (Vp), S – wave velocities (Vs), densities and poisson's ratios of an aquifer at 1300 m (MDRKB) in a well within the North Sea. These various elastic properties were further used for the AVA modelling. (a) The reservoir (marked by blue shade) was initially filled with brine. Gas and then oil was replaced (Gassmann 1951) above a modelled fluid contact to obtain changes in the effective elastic properties. (b) The reservoir was assumed to be filled with oil, and subsequently replaced by gas above the modelled fluid contact. The water lines in the reservoir section within each property graph were plotted as reference.

Fig. 6. (**a**) 2D seismic line AMR_NBR08-135652 passing through well 7117/9-1. The location of this line is highlighted on Fig.1. (**b**) Same seismic line with interpretation. The quartz (red) and opal-CT (purple) percentages from XRD data are plotted along the well track.

Fig. 7. (**a**) Composite section of 2D seismic lines AMR_NBR08-135652 and AMR_NBR09-220403. The opal-A to opal-CT and opal-CT to quartz interfaces do not extend towards the northwest (from well 7117/9-1 to well 7117/9-2). (**b**) Map showing location of the composite section (yellow line) superimposed on the TWT map of Top Sotbakken Group generated from interpretation of the available seismic lines.

Fig. 8. Relation between mineralogy and physical properties of the Sotbakken Group section in well 7117/9-1. The transformation from opal-A to opal-CT, and from opal-CT to quartz generated hard events resulting in flat spots. The black arrow represents the inflection point in the resistivity curve. The figure is modified after Roaldset & He (1995).

Fig. 9. (**a**-**d**) SEM back-scattered images of samples taken from the core in well 7117/9-1 below the Opal-A to Opal-CT transition (see Fig. 7). Mudstone texture showing Opal-CT granular spheres with uneven surface possibly due to growth of crystobalite and tridymite blades. In (**b**), an erect filamentous microbial (EFM) type opal-A, and pyrite overgrowth are present. Voids are common in the chert, which is mainly composed of the opal-CT mineral. (e) A core photograph (from NPD 2018) with a white rectangle indicating the depth at which the sample for slide (b) was taken. Symbols: EFM; Erect Filamentous Microbial type opal-A, CT; Opal-CT and P; Pyrite.

Fig. 10. (**a**) Density-Vp cross plot of Sotbakken Group data from wells 7117/9-1 and 7117/9-2. (**b**) Same cross plot colour-coded with present-day temperature. The well 7117/9-1

demonstrates relatively higher density and Vp compared to well 7117/9-2, as the Sotbakken Group section is deeper and exposed to higher temperature.

Fig. 11. (**a**) Density-Vp cross plot of Sotbakken Group data from well 7117/9-1 colour-coded with depth. (**b**) Same cross plot colour-coded with paleotemperature. The lines show the cluster trend, whereas the red arrow indicates the interval where both density and P- wave velocity decrease with depth and temperature. (**c**) Density-Vp cross plot of Sotbakken Group data from the well 7117/9-2 colour-coded with depth. (**d**) Same cross plot colour-coded with paleotemperature. The density and Vp decrease with depth and temperature. Since the 17-1/2" hole was over-gauge in well 7117/9-2, only data with caliper values below 19" diameter has been plotted.

Fig. 12. (**a**) Density-Vp cross plot of Sotbakken Group data from the well 7117/9-1 colour-coded with quartz%. (**b**) Same cross plot colour-coded with opal-CT%. The change in data trend at knee points indicate transformation of opal-A to opal-CT and then opal-CT to quartz. The red arrow shows the facies where both density and P-wave velocity decrease with depth and increase in opal-CT (b).

Fig. 13. (**a**) Acoustic Impedance (AI)-Deep Resistivity (HRD) cross plot of Sotbakken Group data from well 7117/9-1 colour-coded with paleotemperature. There are three trends in the data. Trend 1 represents an increase in deep resistivity with increasing acoustic impedance initially due to mechanical, followed by chemical compaction resulting in a "hard zone" due to co-existence of both opal-A and opal-CT represented by the culmination point. Trend 2 shows decrease in resistivity with decreasing acoustic impedance as opal-A to opal-CT transformation continue and the water expelled causing an overpressure as depth increases. In trend 3 the deep resistivity is increasing with increase in acoustic impedance that possibly starts with the opal-CT to quartz conversion and keep increasing with further cementation due to increase in depth and temperature. (**b**) Similar cross plot from well 7117/9-2. Trend 1 is absent in this well, whereas the trend 2 depicts the interval where both AI and resistivity decrease with depth, indicating possible overpressure. Trend 3 represents the onset of opal-CT to quartz conversion at the base of the Sotbakken Group.

Fig. 14. (**a**) Amplitude vs. angle (AVA) plot showing both the opal-A to opal-CT and opal-CT to quartz interfaces exhibiting a weak Type-1 signature. In case of the gas-brine, oil-brine and gas-oil contacts there is a weak positive gradient i.e. the amplitude increase with increasing angle. (b) On the Intercept-Gradient plot the opal-A to opal-CT and opal-CT to quartz points plot on the background wet trend, however the fluid interface points fall in quadrant-I.

Tables

Table 1. *Exhumation estimates from various authors*

Exhumation estimates	Well 7117/9-1 (m)	Well 7117/9-2 (m)
Riis *et al*. 1992	405	374
Ohm *et al*. 2008	0	<100
Henriksen *et al.* 2011	0	0
Baig *et al.* 2016	250	460
Ktenas *et al*. 2017	1000	~1000

Table 2. *Paleotemperature from vitrinite reflectance*

Well	Depth (MD)	Vitrinite Reflectance (VR)	No. of Readings	Paleo-temperature	Paleo-gradient	Present-day temperature
	m	% Ro		°C	°C/ km	°C
7117/9-1						
	1400	0.42	25	60.5	36.1	45.4
	2705	0.67	8	103.7		93.8
7117/9-2						
	2010	0.49	22	74.7	34.2	65.7
	2500	0.66	11	102.3		83.4
	3120	0.83	11	123.4		105.7
	3600	1.02	16	142.5		123
	4200	1.25		161.3		144.5
	4800	1.65	13	186.9		166.1

Table 3. *Temperature at the base and top Sotbakken Group*

Well	Depth (MD) m	Paleo Temperature °C	Paleo gradient °C/ km	Present temperature °C
7117/9-1				
	1139	44.3	36.1	35.6
	1809	68.4		60.4
7117/9-2				
	1092	47	34.2	32.7
	1375	56.7		42.9

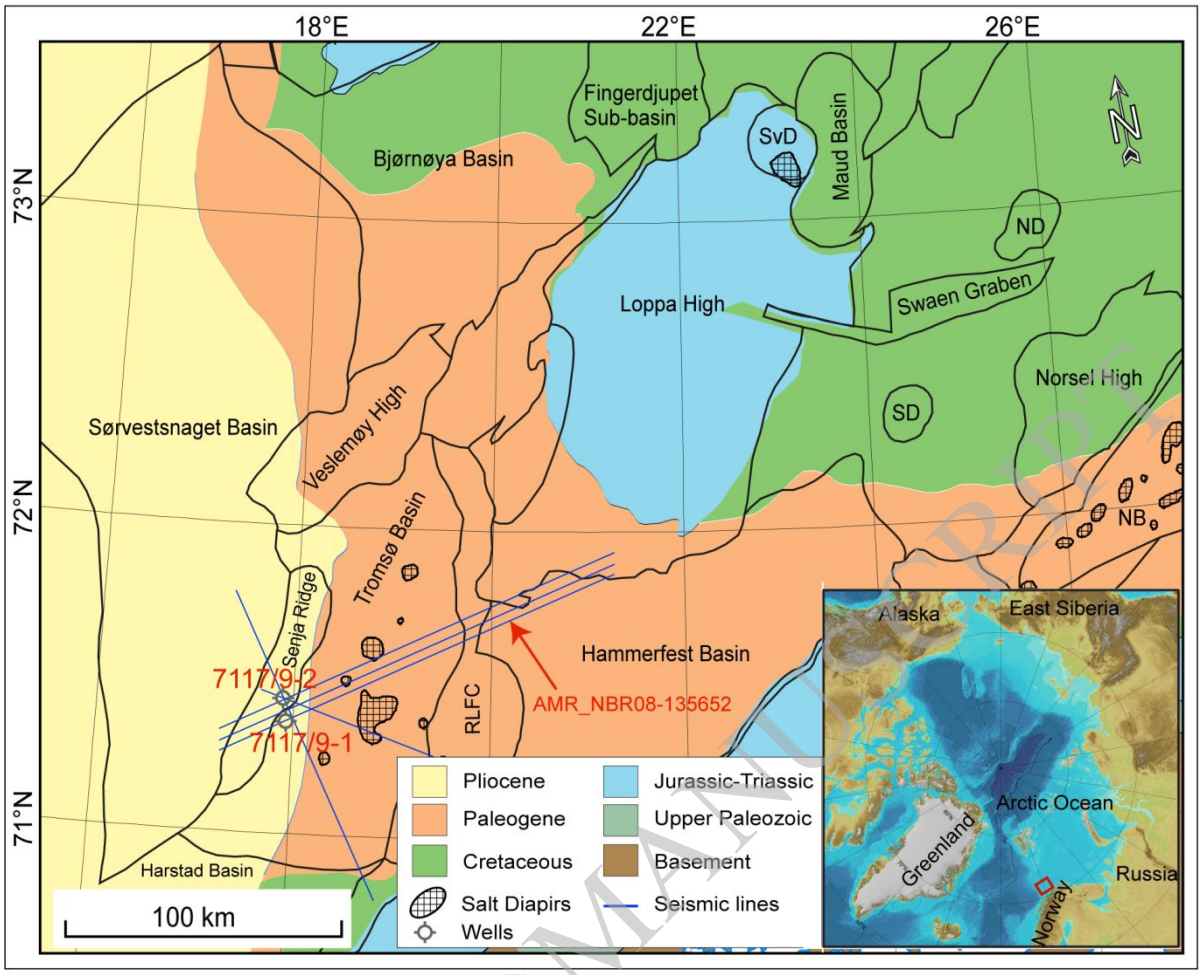

Fig. 1

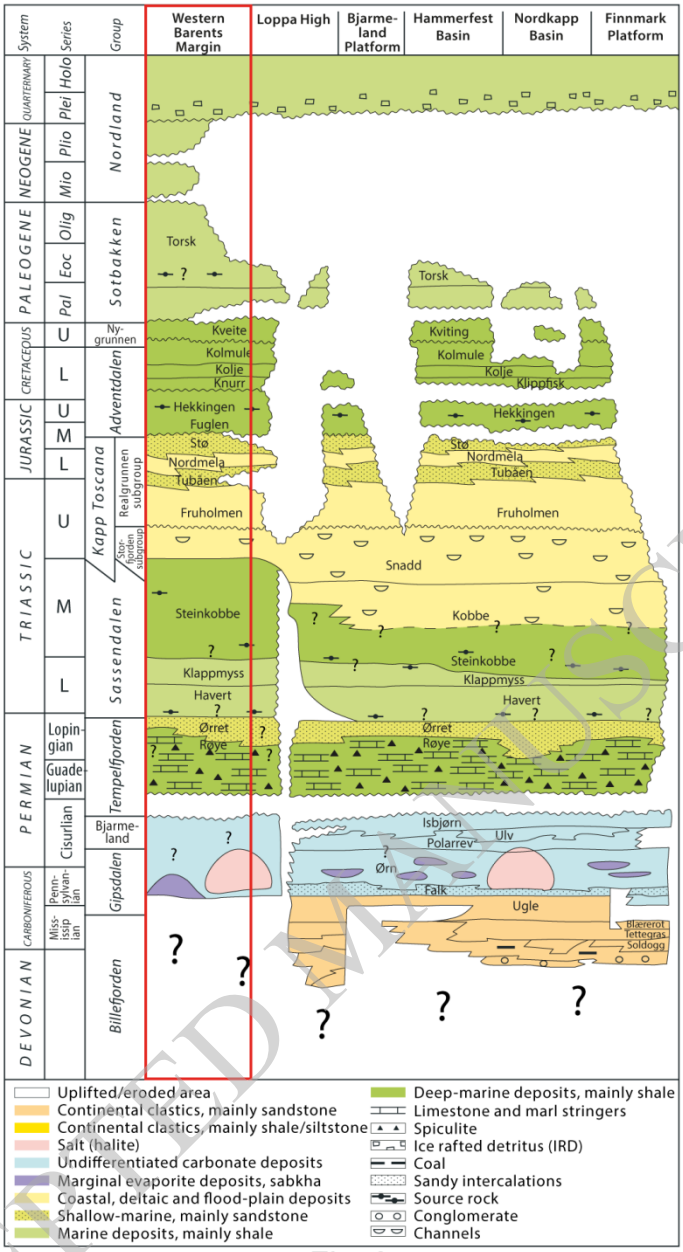

Fig. 2

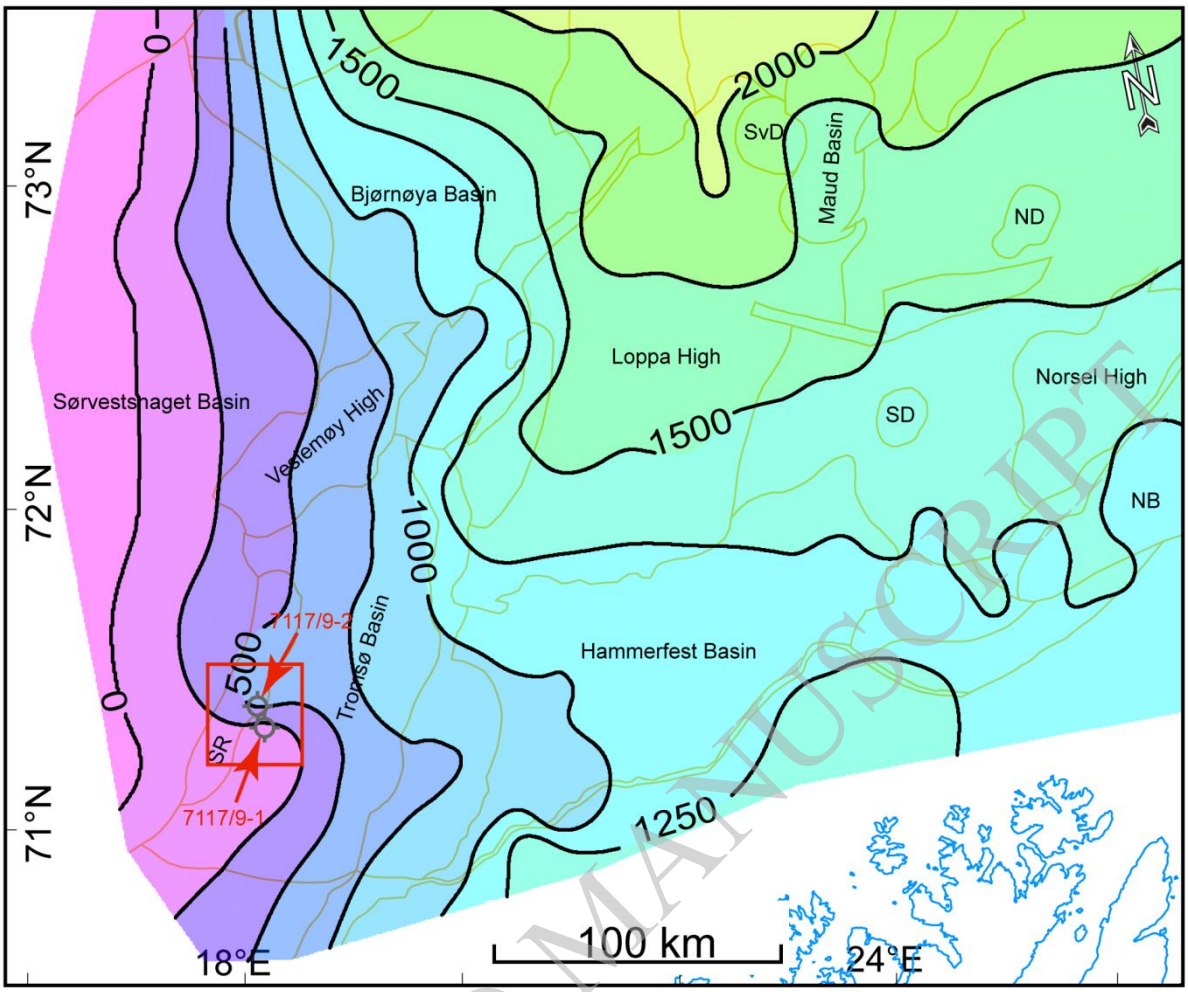

Fig. 3

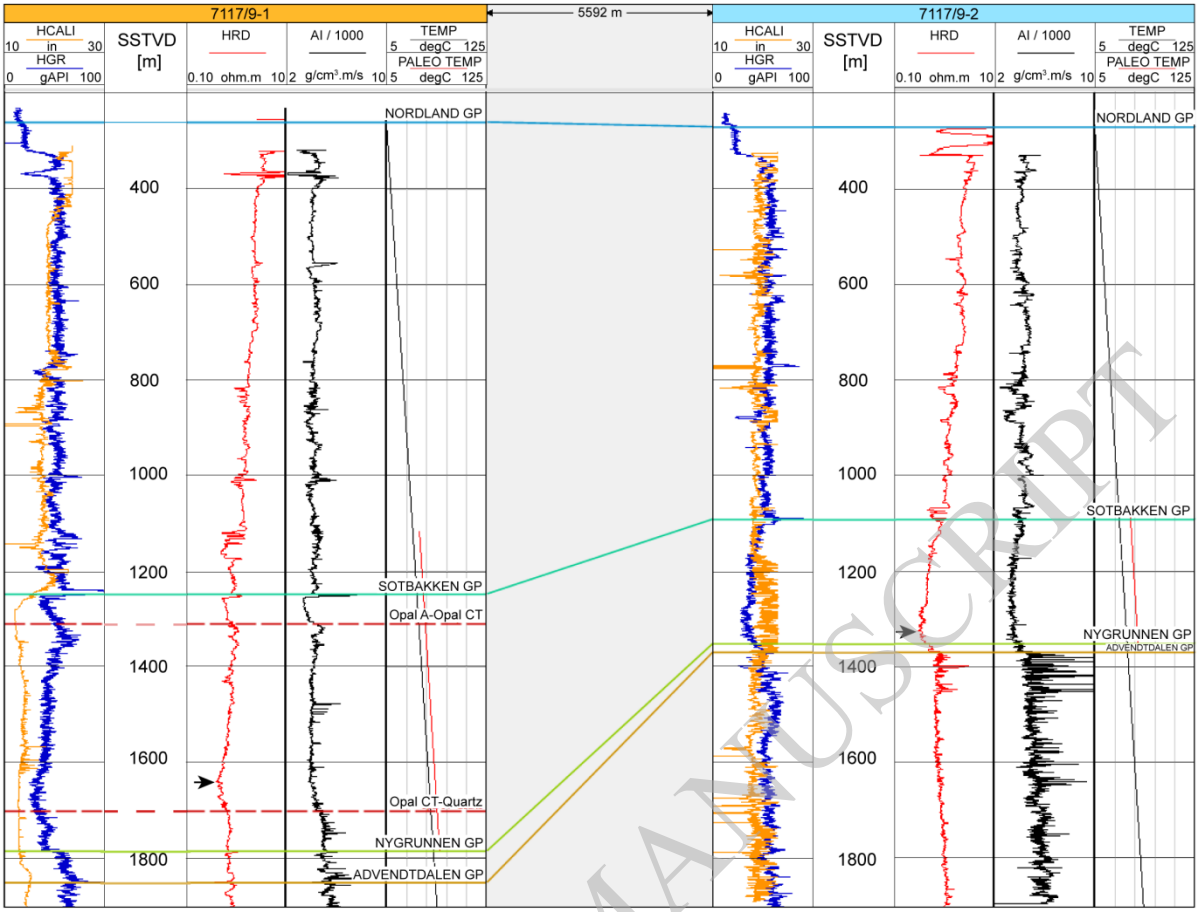

Fig. 4

a)

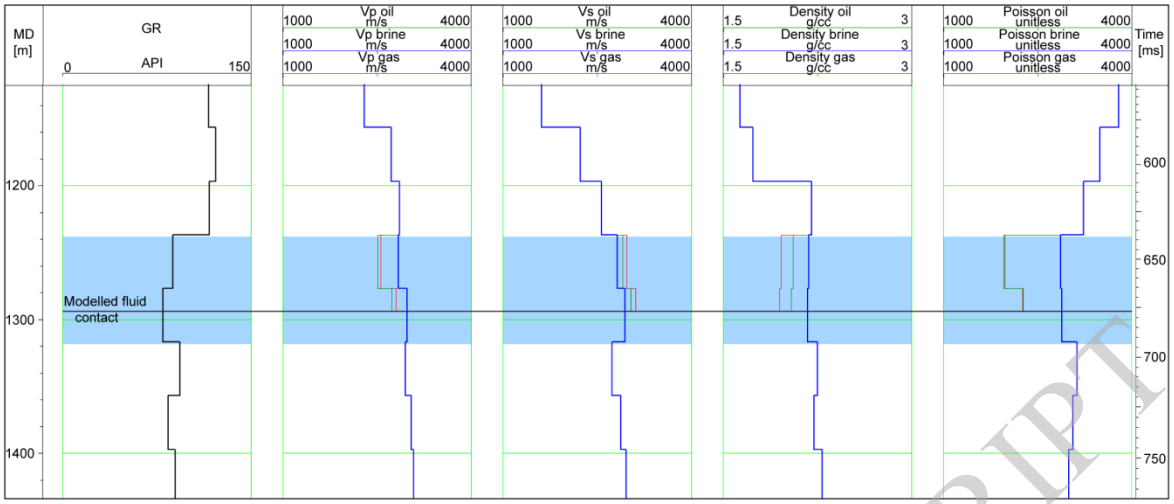

b)

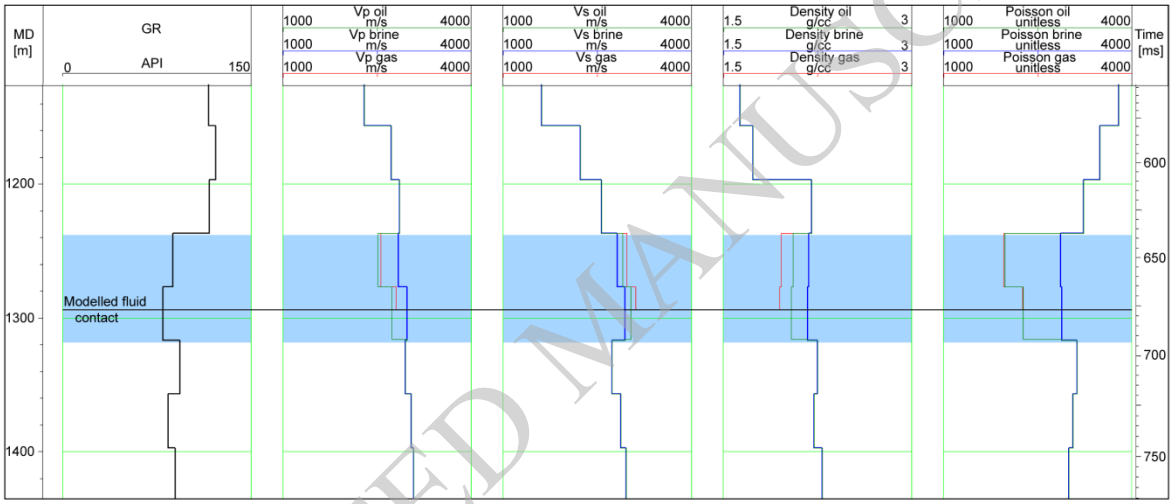

Fig. 5

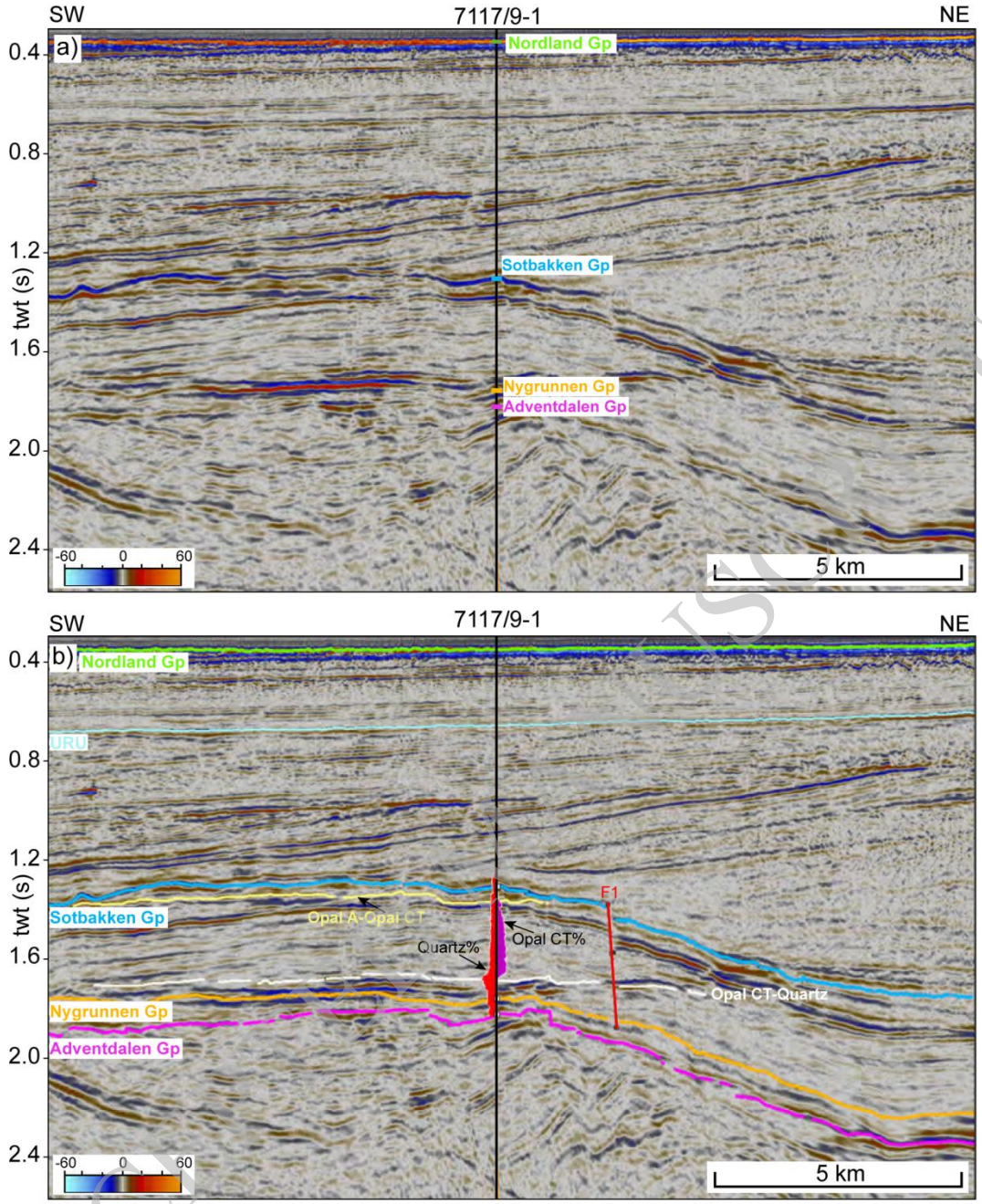

Fig. 6

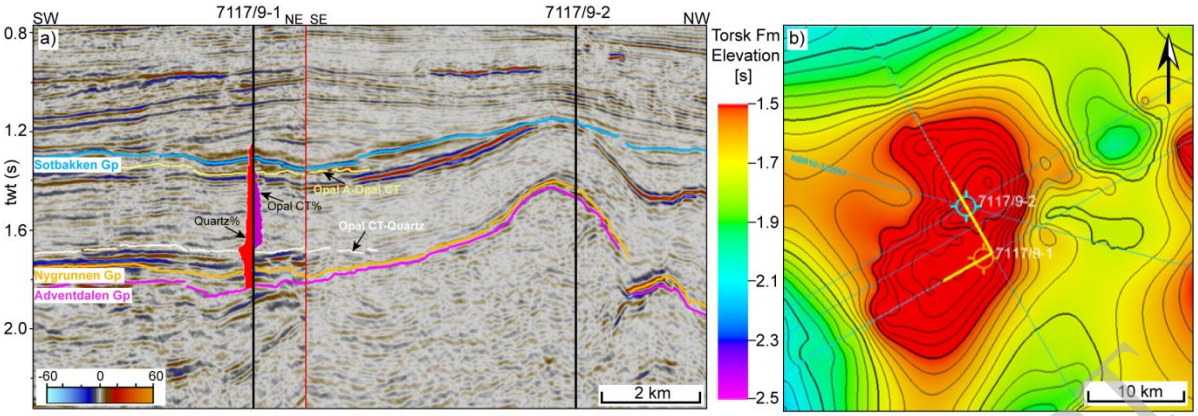

Fig. 7

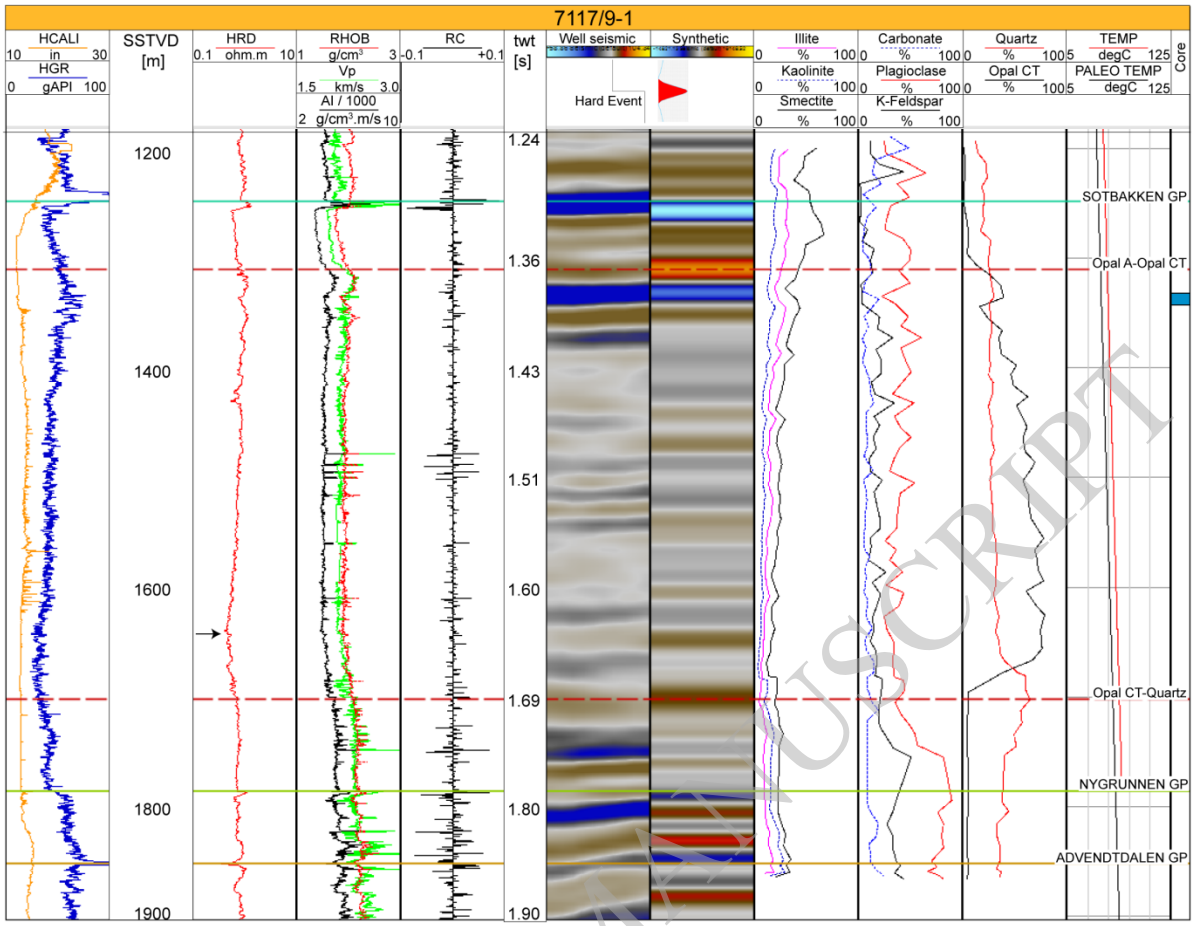

Fig. 8

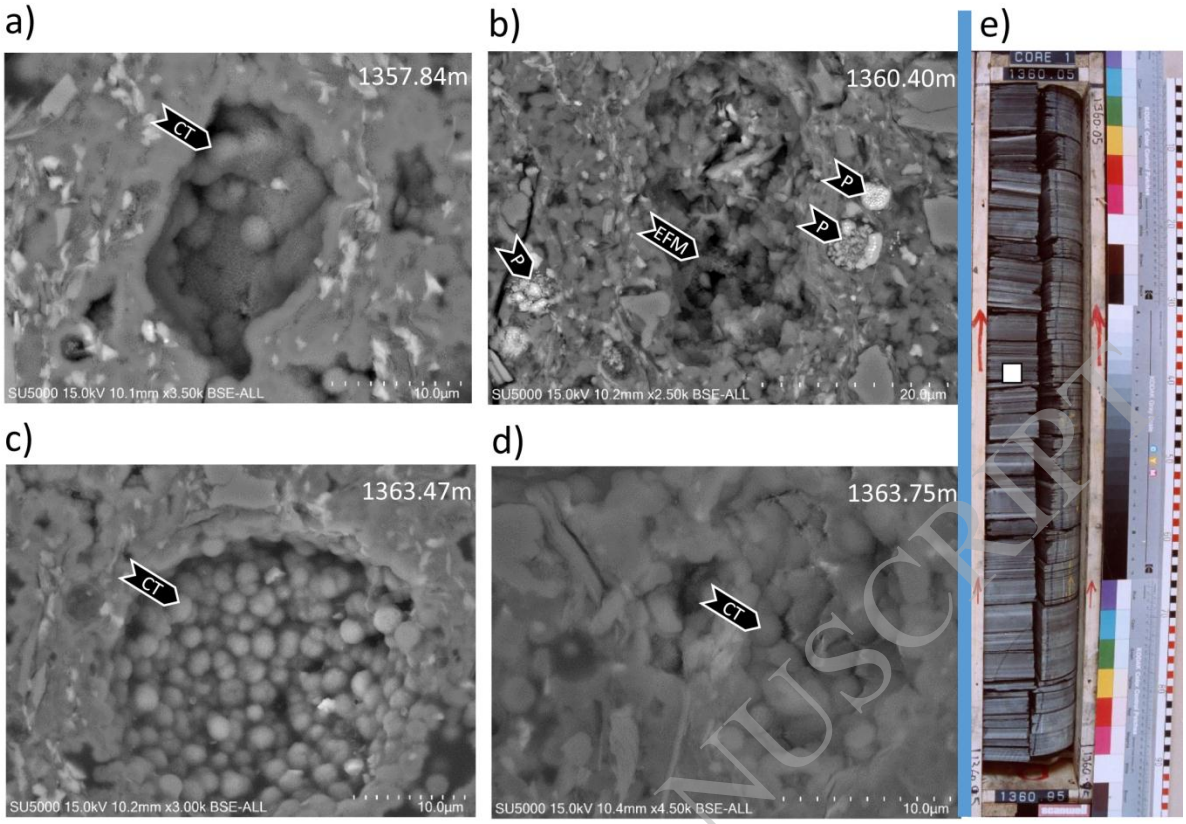

Fig. 9

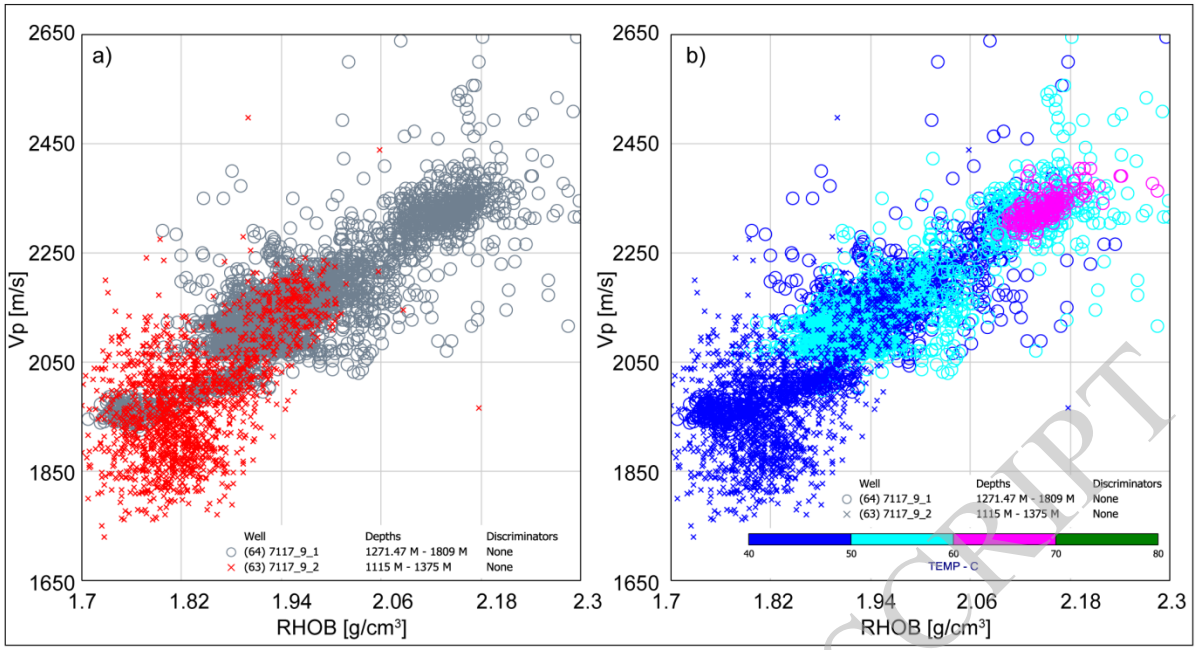

Fig. 10

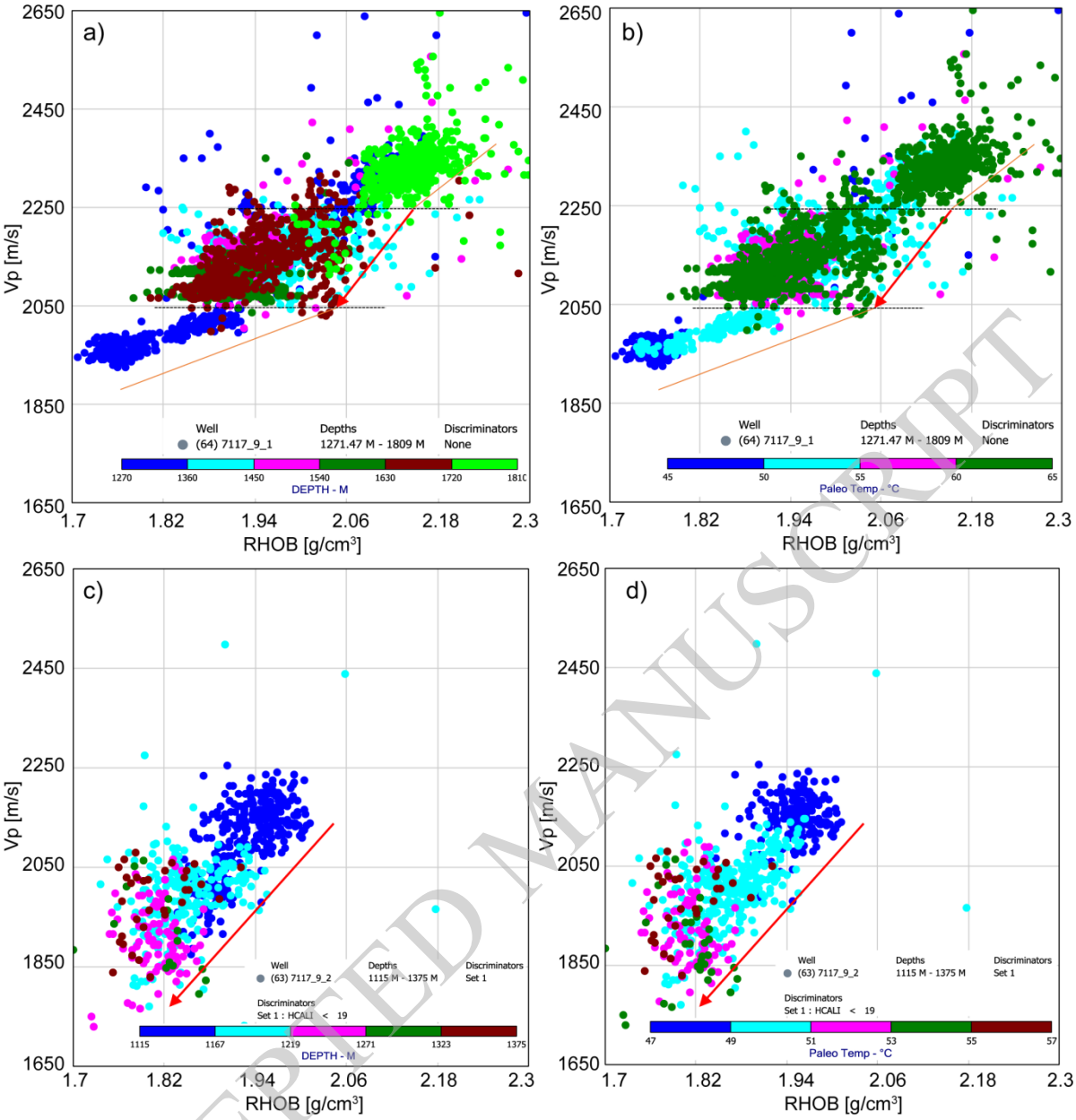

Fig. 11

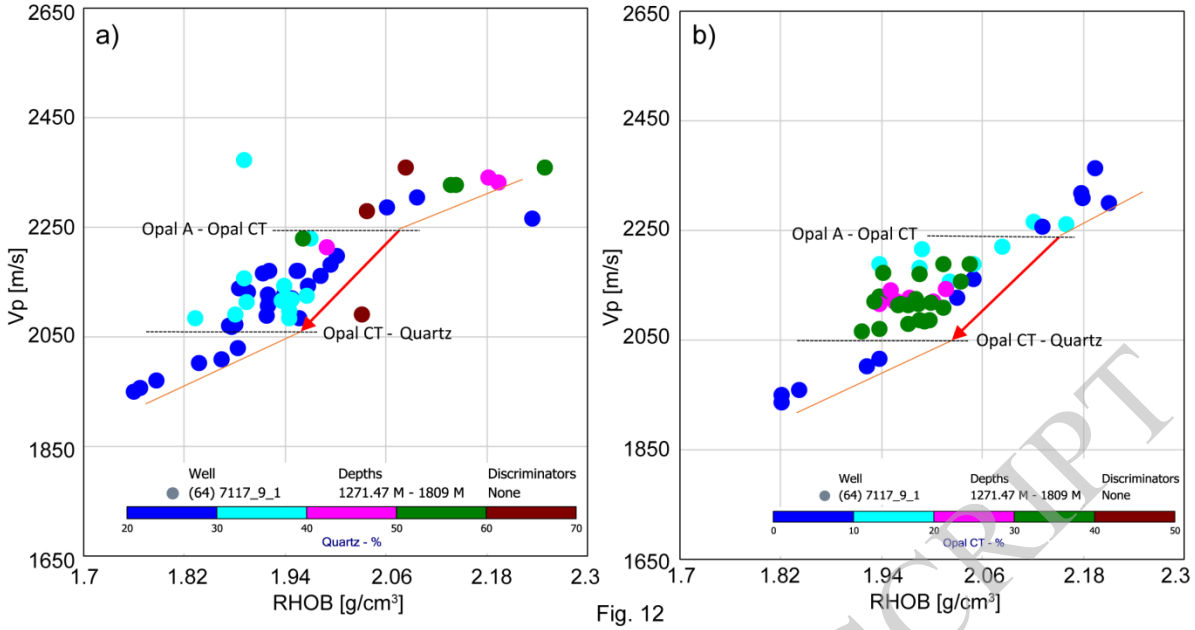

Fig. 12

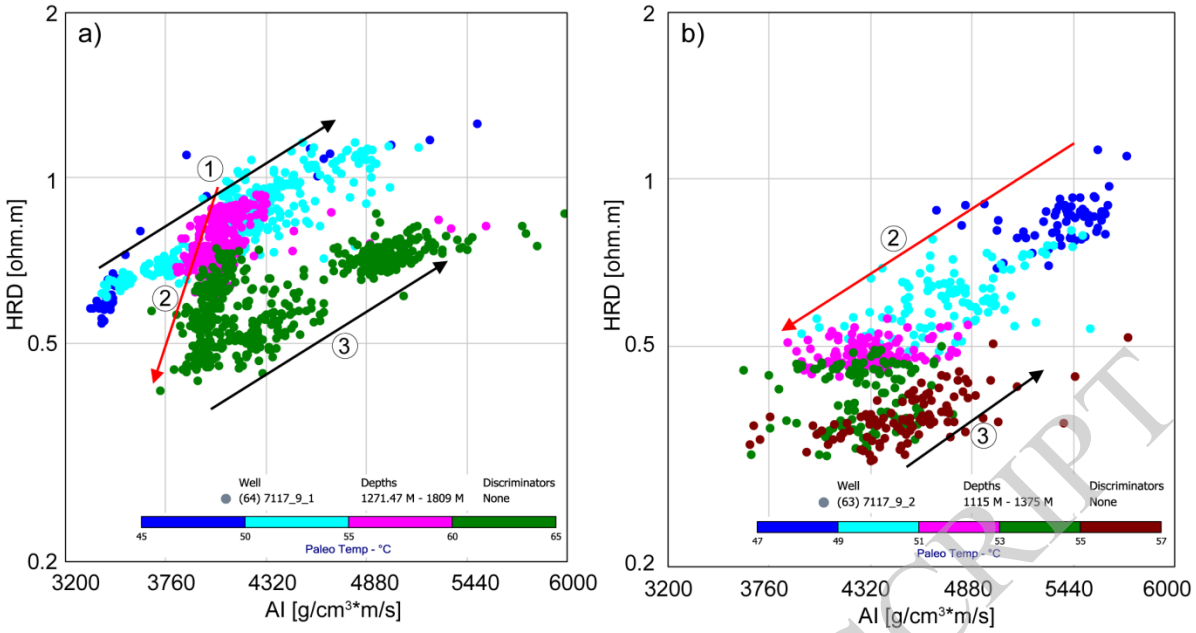

Fig. 13

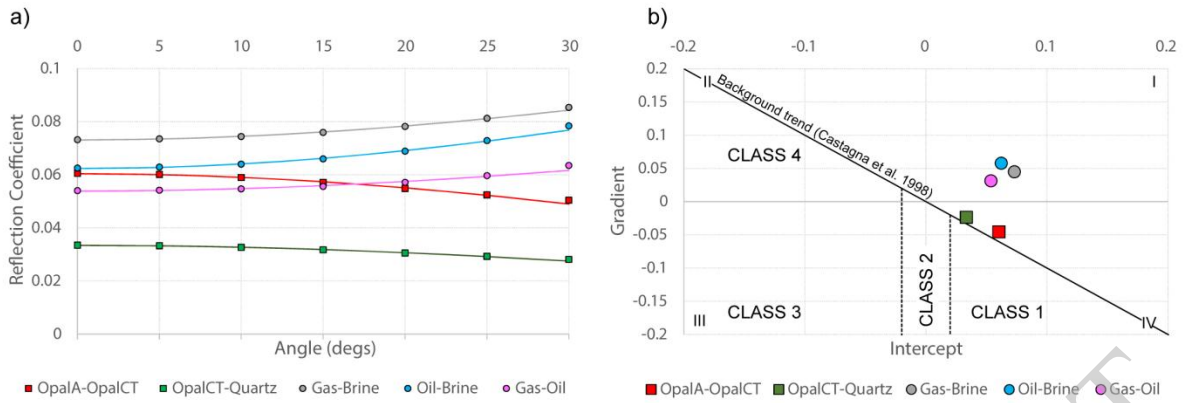

Fig. 14